

IMAGING TECHNIQUES FOR TRANSVERSE BEAM-PROFILE/SIZE MONITORS*

Alex H. Lumpkin[#], Fermi National Accelerator Laboratory, Batavia, IL 60510 USA

Abstract

A short review of imaging techniques for transverse beam size monitors is presented. Considerations on the choice of converter mechanism, whether scintillator or optical transition radiation (OTR) are discussed. Examples are presented based on low-energy tests at the Fermilab A0 photoinjector and are planned for the Advanced Superconducting Test Accelerator at Fermilab. Issues for imaging noninterceptively with optical diffraction radiation and for non-relativistic beams with OTR are also described.

INTRODUCTION

The characterization of transverse beam profile/size by imaging relativistic beams using intercepting screens based on scintillators or optical transition radiation (OTR) is a well-established technique at many accelerators [1-3]. There are several considerations in choosing the conversion mechanism including beam size, charge, beam energy, beam power, pulse structure, presence of microbunching instability effects, etc. Examples will be given for the fundamental contributions to system resolution including the scintillator screen resolution (powder thickness and single crystal effects), optical depth-of-focus aspects, and the OTR polarization and point-spread-function effects. The imaging techniques can be extended to the non-intercepting arena using optical diffraction radiation (ODR) [4-6]. Beam-size results and proposed ODR experiments at 23 GeV will be described. In addition, the feasibility [7] and first OTR imaging results on non-relativistic 11.4 MeV/u Uranium ions at GSI, Darmstadt, Germany will be presented [8].

BEAM-SIZE IMAGING CONSIDERATIONS

A basic particle beam imaging system includes as shown in Fig. 1:

- a **conversion mechanism**: (scintillator, optical or x-ray synchrotron radiation (OSR or XSR), optical transition radiation (OTR), Cherenkov radiation (CR), undulator radiation (UR), and optical diffraction radiation (ODR),
- **optical transport** (windows, lenses, mirrors, filters, polarizers),
- **imaging sensor** such as a CCD, CID, CMOS camera with or without image intensifier and/or cooling,
- **video digitizer** (built in or external), and an
- **image processing software**.

[#] lumpkin@fnal.gov

*Work supported under Contract No. DE-AC02-07CH11359 with the United States Department of Energy.

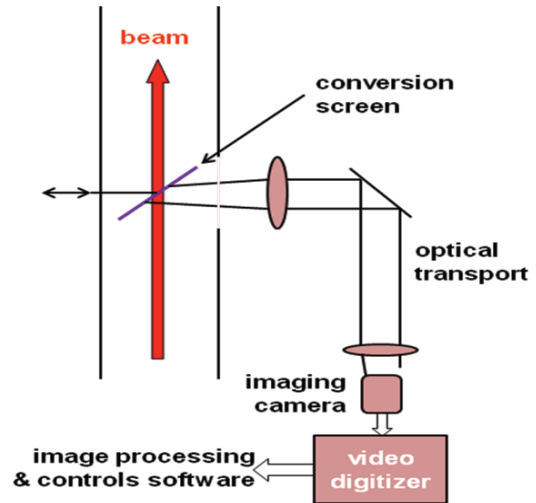


Figure 1: Schematic of beam-imaging system.

We then have to identify corrections to consider in our analysis of the beam image. The system related ones are: YAG:Ce powder and crystal screen resolution, OTR polarization effects, OTR point spread function, camera calibration factor, and finite slit size (if applicable). The accelerator and beam-related effects include the beta star term in the dispersive plane of a spectrometer and the macropulse blurring effects due to RF power or phase slew on beam size, energy spread, and beam divergence in OTR images that sum over many micropulses.

Uncorrelated terms are treated as a quadrature sum (see Lyons' textbook [9]) which contribute to the observed image size (Obs) including the actual image size (Act), YAG screen effects (YAG), camera resolution (Cam), and finite slit width (Slit) as shown in Eq. 1. In addition there can be macropulse effects and OTR polarization effects.

$$Obs^2 = Act^2 + YAG^2 + Cam^2 + Slit^2 \quad (1)$$

and solving for the actual beam size, we have

$$Act = \sqrt{Obs^2 - YAG^2 - Cam^2 - Slit^2} \quad (2)$$

A series of experiments has been performed at the A0PI facility which is shown schematically in Fig. 2. The imaging cross stations are indicated as X# and most of the work was done at X3, X5, X23, X24, and the prototype station indicated. The facility operates with a photocathode RF gun followed by a superconducting L-band 9-cell cavity generating final beam energies of 13-15 MeV, with micropulse charges of 250 to 1000 pC [10].

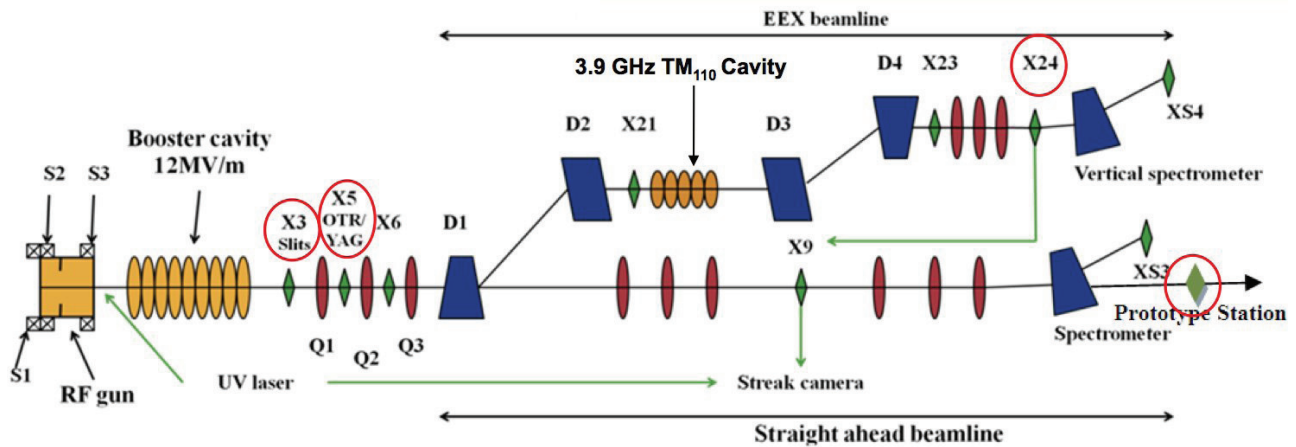


Figure 2: A schematic of the AOPI facility with PC rf gun, superconducting booster cavity, diagnostics cross stations, the spectrometers, and EEX beamline.

Beam Profiling with YAG:Ce Scintillator Screens

YAG:Ce powder screens used at the A0 Photoinjector had nominally a 5- μm grain size and were coated at 50- μm thickness on various metal 1-mm-thick substrates of Al or SS. In the AOPI arrangement the scintillator material was on the front surface of the substrate, and oriented at 45 $^\circ$ to the beam direction. The powder screens were kindly provided by K. Floettmann (DESY). Observed characteristics include the response time of about 80 ns FWHM, and there have been reports of saturation of the mechanism for incident electron beam areal charge densities $\sim 10 \text{ fC}/\mu\text{m}^2$. This latter effect can cause a charge dependence of the observed image size in addition to the low-charge, screen-resolution limit. The initial comparison tests of the powder screens and OTR were done at X5. As shown in Table 1 the scintillator-based sizes are insensitive to the linear polarizer while the OTR x size is reduced by 23 μm out of 125 with the vertical polarizer. The deduced powder resolution term for this case is $80 \pm 20 \mu\text{m}$ using the polarized OTR as the reference size, and the average of three separate measurements is $60 \pm 20 \mu\text{m}$.

Table 1: Comparison of OTR and YAG:Ce Screens at X5

Screen Type	No. of Bunches	X5 Linear Polarization	Fit σ (pixels)	X size (μm)
OTR	10	none	5.49 ± 0.05	124.5
	10	vertical	4.47 ± 0.09	101.0
YAG:Ce	1	none	5.67 ± 0.05	128.7
	1	vertical	5.71 ± 0.04	129.6

These powder screens were replaced by 100- μm thick single crystal YAG:Ce screens oriented normal to the beam followed by a 45 degree mirror. A summary of various tests of powder samples and single-crystal YAG:Ce is shown in Fig. 3. It is obvious that the resolution term for powder screens is thickness dependent

and much larger than the grain size. It is also clear that the 100- μm thick single crystal normal to the beam provides better resolution than a powder screen of similar thickness. The material and screen orientation are given in the label near each datum [11].

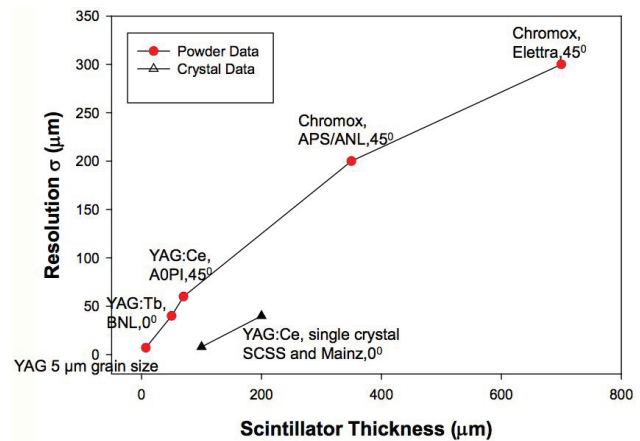


Figure 3: A comparison of deduced resolution terms for powder screens and YAG:Ce crystals.

OTR Imaging

The fundamental OTR mechanism occurs when a charged particle beam transits the interface between two media. The approaching charge and the induced image charge in the second medium may be treated as a collapsing dipole with the consequent emission of radiation, i.e. OTR. The yield is about 1 visible photon per 1000 electrons incident, but they are emitted in the few-fs time scale as opposed to the slower 80-ns scintillation process in the previous section. The radiation is emitted around the angle of specular reflection for backward radiation and around the angle of the beam direction in the forward direction for high gamma beams. For an oblique incidence such as 45 degrees, backward OTR is emitted at 90 degrees to the beam direction as shown at the upper right of Fig. 4. This geometry is compatible with most accelerator beam profiling stations.

Copyright © 2012 CC-BY-3.0 and by the respective authors

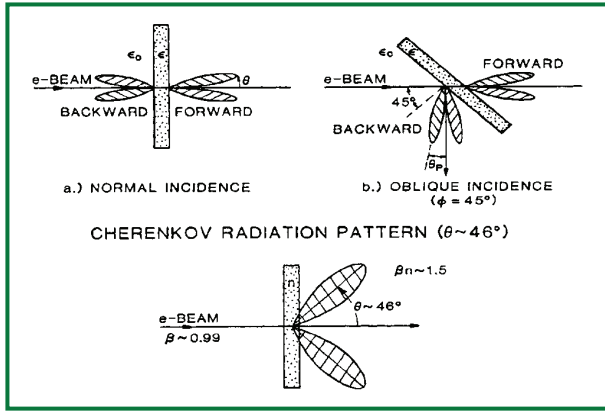


Figure 4: A schematic of OTR emission at the boundary of two media compared to Cherenkov radiation [2].

As comparison, the Cherenkov radiation cone angle is much larger at about 46 degrees for $\beta n=1.5$, where β is the particle velocity over the speed of light and n is the index of refraction of the medium.

The OTR angular distribution pattern is annular with an opening angle of $1/\gamma$, where γ is the Lorentz factor. The peak intensity goes roughly as $1/\gamma^2$ and the spectral function as $1/\lambda^2$. The visibility of the central minimum depends on the beam divergence and is therefore related to beam transverse emittance. This visibility feature for OTR from a single foil is usable for divergence sensitivity down to about 10% of $1/\gamma$.

OTR Polarization and PSF Effects

During the course of our experiments with linear polarizers placed in the optical transport to the camera at the prototype station, we observed the OTR beam image size was smaller when we used the perpendicular polarization component relative to the beam dimension as shown in Fig. 5. The total OTR image is at the upper left, and the vertically polarized image is at the upper right. The fits to the projected x profiles gave sigma values of $66.8 \pm 0.3 \mu\text{m}$ and $55.1 \pm 1.1 \mu\text{m}$, respectively. This effect at the 15-20% level at $55 \mu\text{m}$ we felt should not be ignored and further investigations are planned.

One possible explanation was to consider the OTR point-spread function that had been identified in the past by Castellano and Verzilov [12]. Basically, one convolves the OTR single electron angular distribution function with the J_1 Bessel function for diffraction from a point source as given in Eq. 3. The function argument involves θ_{max} , γ , and $\zeta = k R_i / M$ (where k is the wave number, R_i is the lens radius, and M is the optical magnification). In this case one actually obtains an annular PSF at the few-micron level using visible light in the image plane.

$$f^2(\theta_{max}, \gamma, \zeta) = \left[\int_0^{\theta_{max}} \frac{\theta^2}{\theta^2 + \gamma^{-2}} J_1(\zeta \theta) d\theta \right]^2 \quad (3)$$

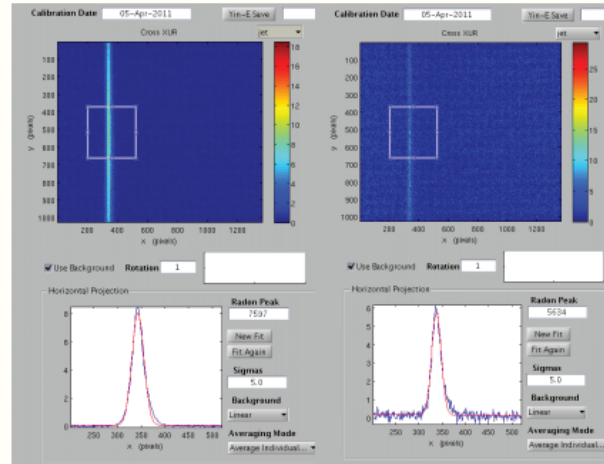


Figure 5: Comparison of the OTR image (left) with the perpendicularly polarized OTR component narrower image (right). The projected profiles are below the images.

In their calculations they assumed a lens aperture of 100 mrad and calculated the total OTR PSF to be about 12λ FWHM. They do calculate different projected profiles for the two polarization components which when convolved with the actual beam size would, in principle, give slightly different observed beam sizes. The effect due to the beam energy is generally small.

As an illustration of the issue, two cases for $E=14.3$ MeV, $M=1$, $\theta_{max}=0.010$ rad, $\lambda=500$ nm, and initial sigmas of 10 and $50 \mu\text{m}$ are shown in Fig. 6. The convolutions of total OTR and horizontally polarized OTR with horizontal and vertical projections with the Gaussian profiles are shown. For these input conditions we see ~10% effects at $50 \mu\text{m}$, and 120 % effects at $10 \mu\text{m}$ for the total PSF. In the experiment we have about a $12\text{-}\mu\text{m}$ image size reduction at $55 \mu\text{m}$ using the perpendicular component compared to the $3\text{-}\mu\text{m}$ -reduction modeled result.

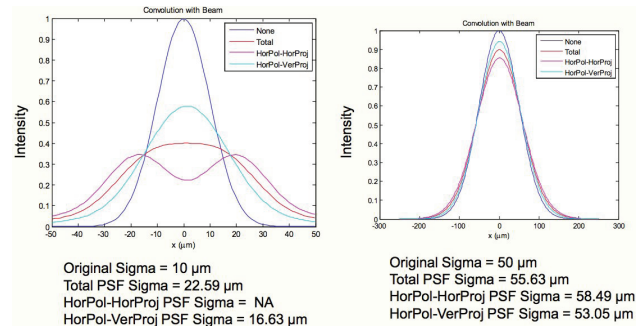


Figure 6: A comparison of the OTR PSFs convolved with two Gaussian beams with sigma = $10 \mu\text{m}$ (left) and $50 \mu\text{m}$ (right).

Microbunching Instability and COTR

One of the recent developments in diagnostics for compressed bright beams is the identification of the longitudinal space charge induced microbunching (LSCIM) instability and the appearance of dominating

coherent OTR (COTR) signals [13,14]. Since this effect is attributed to noise fluctuations in the beam as it transports through the accelerator, the observed effects are random in spatial distribution and their local intensities preclude simple beam-profile measurements. The effect is described by Ratner et al. [15], and the broad band nature of the gain is shown in Fig. 7 for the nominal LCLS case of a 3-keV slice energy spread. We have superimposed the CCD camera response curve and the incoherent OTR spectral distribution on the plot to illustrate the relationships.

It has been demonstrated as shown in Fig. 8 that by choosing the violet spectral region (such as indicated by the rectangle centered at 400 nm in Fig. 8), one can reduce the LSCIM COTR and still have some OTR signal. This can be made even more advantageous by using a scintillator that emits in the violet regime such as LSO:Ce at 415 nm. In addition, options to image in the ultraviolet down to 200 nm or even in the EUV appear feasible, and temporal gating to reject prompt COTR versus delayed emissions of scintillators can also be effective whether by a microchannel plate intensifier [16] or by the digital CCD camera shutter [17].

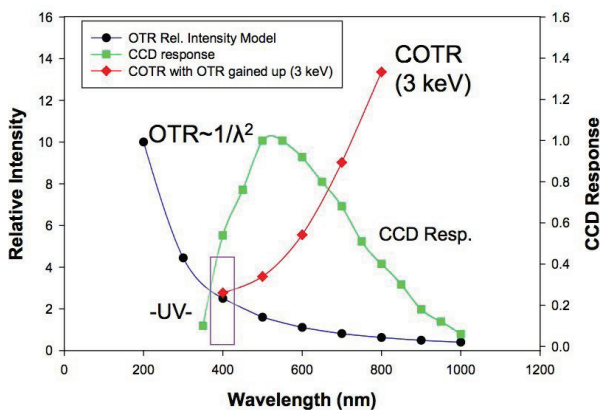


Figure 7: A comparison of the spectral dependence of incoherent OTR and LSCIM COTR with the CCD response [11].

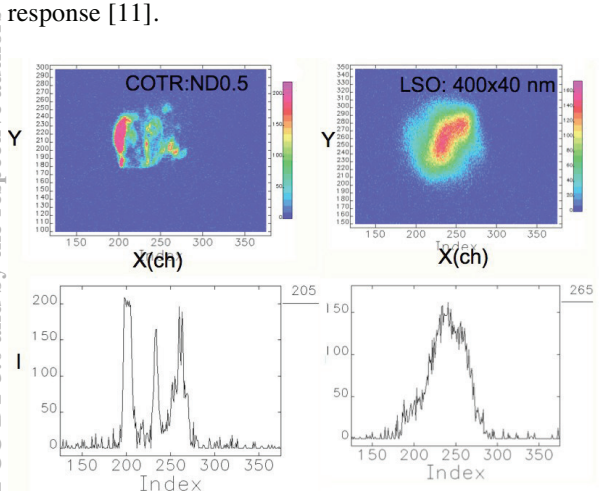


Figure 8: A comparison of the COTR image (left) with the violet filtered LSO:Ce image (right). The projected x profiles are below each image, respectively.

NON-INTERCEPTING ODR IMAGING

The techniques above rely on beam-intercepting screens and are used for low-power beams. For relativistic beams one can consider ODR imaging as a non-intercepting beam-size monitor. An initial demonstration at KEK used the scan of the angular distribution of ODR from a slit aperture with a very low divergence beam so they determined beam size sensitivity in the intensity valley between the angular distribution lobes [4]. Recently, a set of experiments extended this technique with two screens and used a sensitive camera for two-dimensional imaging [6].

Another option involves direct near-field imaging of the polarized components of ODR [5]. The initial measurements were done at ANL using a 7-GeV beam energy and a flat beam with horizontal size about 1300 μm and vertical size of 200 μm . The metal screen or ODR converter was inserted vertically by a stepper-motor-controlled actuator. The key scaling of $\gamma\lambda/2\pi$ was 1.4 mm and the distance from beam center to screen edge was varied from 1 to 3 mm. Under such conditions a standard CCD camera had sufficient sensitivity to see the ODR from a single 3.3-nC micropulse as shown in Fig. 9. The techniques were also demonstrated via collaborations at CEBAF/JLAB at 4.5 GeV [18] and at FLASH at 800 MeV on bunch trains which allowed integration over 10s of nC [19]. The next phase is the proposed tests at 23 GeV on the FACET/SLAC where micropulse charges of 3 nC and beam sizes down to 10 μm are expected [20].

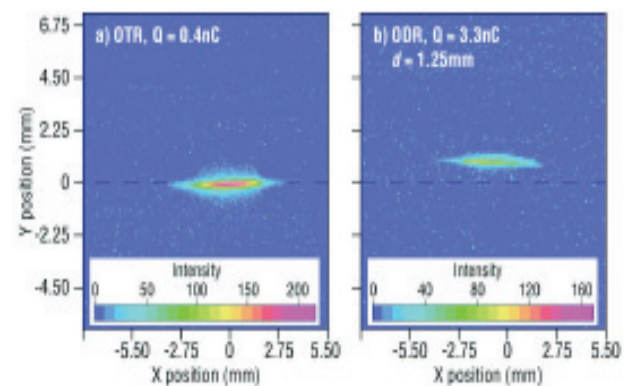


Figure 9: A comparison of a) the OTR image with the screen edge 4 mm below the beam center and b) the ODR image with the screen edge 1.25 mm above the beam center. The induced currents in the metal radiate visible photons in both cases. The beam energy at ANL was 7 GeV [5].

NON-RELATIVISTIC BEAM IMAGING

Almost all of the OTR experiments for the last few decades have been on relativistic beams, whether electron, proton, or antiproton. For linac-based cases, the CLIC tests with 80-keV electrons showed the aspects of low- β work [21]. During a visit to the heavy ion facility at GSI in Darmstadt, Germany this author identified the

possibility of OTR imaging of high charge-state ion beams [7]. In this case one takes advantage of the OTR's yield scaling with $\beta^2 Q^2$, where Q is the charge state of the ion [22]. A schematic of the concepts is shown in Fig. 10. The key features are the ion beam intensities and charge states, a thin metallic OTR converter screen, the altered angular distribution lobes for low-beta particles, and a sensitive camera system. Obviously in the case of U^{+28} or U^{+73} ions the charge state is a strong multiplier on the photon number. There is a trade on ion number and charge state for lower atomic number cases.

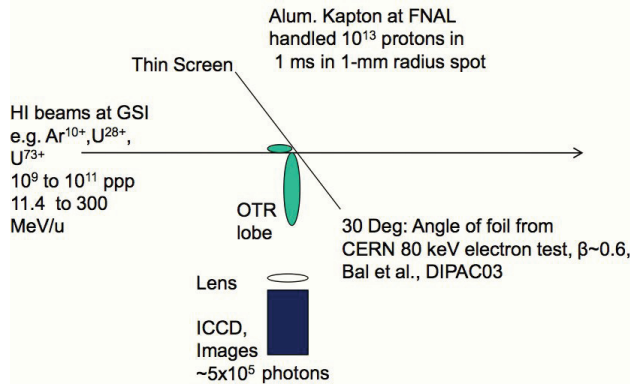


Figure 10: A schematic of the HI OTR imaging technique showing the key aspects of ion number, charge state, thin foil, adjusted angle for low β , and ICCD [7].

The first successful experiments are being reported in this workshop in more detail in a separate paper [8], but one of the first OTR images of U ion beams is shown in Fig. 11. In Fig. 12 the effect of the charge state is quite clearly demonstrated where the +73 state image is indeed about 6.7 times brighter than the +23 state for the same number of ions, 7×10^8 .

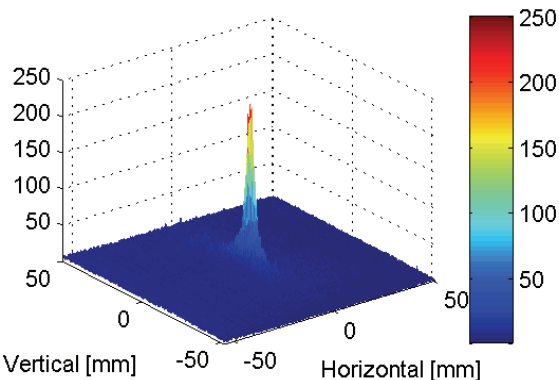


Figure 11: Initial imaging of the Uranium ion beam at 11.4 MeV/u at GSI; the figure shows the pseudo 3D display [8].

Another key requirement of the imaging method is to show signal linearity with the bombarding beam intensity. This is shown in Fig. 12 over a factor of 10 particle intensity range. Based on these promising results further studies are planned, and the evaluation with other ion species and energies will be considered.

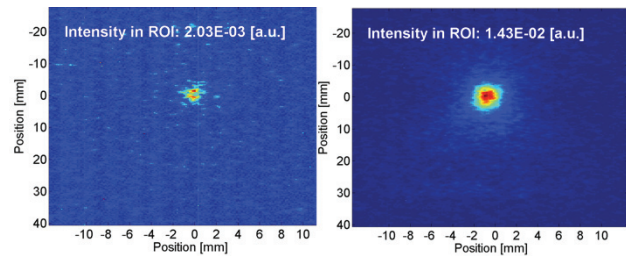


Figure 12: A comparison of the U ion +28 charge state OTR image (left) with the +73 charge state (right) for the same particle number [8].

The technique also should be applicable to the planned upgrade at GSI, the Facility for Antiproton and Ion Research (FAIR), with its expected higher energies and intensities. The foil robustness still needs to be addressed with different beam intensities, and there probably will be a limit imposed to preserve the foils.

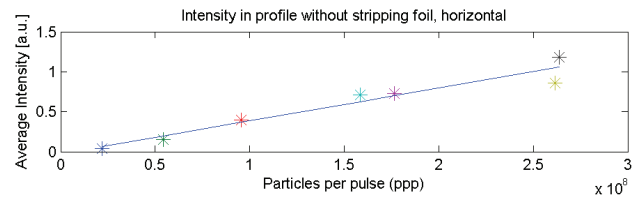


Figure 13: Plot of the OTR signal versus particle number showing clear linearity in this regime [8].

SUMMARY

In summary, a description of various correction terms for beam profiling with intercepting scintillation and OTR screens has been provided. The OTR PSF and polarization effects were also presented with a recommendation of using the perpendicular polarization component for each transverse dimension. There is also the possibility of using the PSF structure in the few-micron beam size domain. The extension to non-intercepting beam size imaging with ODR was briefly described. Finally, a new paradigm for imaging non-relativistic heavy ions has been reported via the GSI collaboration. Applicability at the Relativistic Heavy Ion Collider (RHIC) is also under discussion. The future indeed remains bright for imaging techniques.

ACKNOWLEDGMENTS

The author acknowledges the support of N. Eddy and M. Wendt of FNAL, the A0PI team, the discussions with D. Rule (NSWC-CD), and collaborations with B. Walasek-Hohne and P. Forck of GSI on HI tests.

REFERENCES

- [1] L. Wartski et al., "Detection of optical transition radiation and its application to beam diagnostics", IEEE Trans. Nucl. Sci. Vol. 20, No.3, (1973) 544.
- [2] Alex H. Lumpkin, "Advanced Time-resolved Imaging Techniques for Electron-beam Characterizations", Accelerator Instrumentation Workshop 1990, AIP Conf. Proceedings No. 229, (1991) 151.
- [3] V. E. Scarpine et al., "OTR imaging of intense 120 GeV protons in the NuMI beamline at FNAL" Proceedings of PAC 2007, THOAC02.
- [4] P. Karataev et al., PRL **93**, (2004) 244802.
- [5] A.H. Lumpkin et al., Phys. Rev. ST-AB **10**, (2007) 022802.
- [6] E. Chiodroni et al., Proc. of DIPAC09, TUOA02, (2009).
- [7] Alex H. Lumpkin, "Feasibility of OTR Imaging of Non-Relativistic Ions at GSI", Proc. of Scintillating Screen Applications in Beam Diagnostics Workshop, GSI, Darmstadt, Germany, Feb. 14-15, 2011; <http://www-bd.gsi.de/ssabd>
- [8] B. Walasek-Hohne, C. Andre, F. Becker, P. Forck, A. Reiter, M. Schwickert, and A. Lumpkin, "Pilot Studies on Optical Transition Radiation Imaging of Non-Relativistic Ions at GSI", TUCP03, these proceedings.
- [9] Louis Lyons, *Statistics for Nuclear and Particle Physicists*, Cambridge Press, (1986).
- [10] T. Koeth et al., Emittance Exchange at the Fermilab A0 Photoinjector, Proceedings of PAC09, Vancouver, Canada, FR5PFP020, JACoW (2009).
- [11] A.H. Lumpkin et al., Phys. Rev. ST-AB **14**, (2011) 060704.
- [12] M. Castellano and V.A. Verzilov, Phys. Rev. ST-AB **1**, (1998) 062801.
- [13] D. H. Dowell et al., Proceedings of FEL07, Novosibirsk, WEAAU01 (2007).
- [14] A.H. Lumpkin et al., Phys. Rev. ST-AB **12**, (2009) 04074.
- [15] D. Ratner, A. Chao, and Z. Huang, Proceedings of FEL08, Gyeongju, Korea, TUPPH041, (2008).
- [16] M. Yan et al., presented at FEL11, Shanghai, China, THPB16 (2011).
- [17] Alex H. Lumpkin, presented at the Microbunching Instability Workshop, College Park MD, April 13, 2012.
- [18] P. Evtushenko et al., Proc. of BIW08, 332 (2008).
- [19] A.H. Lumpkin et al., Proc. of BIW08, TUPTPF061 (2008).
- [20] A.H. Lumpkin et al., Proc. of PAC11, MOP220 (2011).
- [21] C. Bal et al., "OTR from Non-relativistic Electrons", Proc. of DIPAC 2003.
- [22] V. L. Ginzburg and V.N. Tsytovich, *Transition Radiation and Transition Scattering*, Adam Hilger Series on Plasma Physics, (1984).